MATERIALS SCIENCE

Crystal critters: Self-ejection of crystals from heated, superhydrophobic surfaces

Samantha A. McBride[1,2], Henri-Louis Girard[1], Kripa K. Varanasi[1]*

Mineral or crystal fouling (the accumulation of precipitants on a material and damage associated with the same) is a pervasive problem in water treatment, thermoelectric power production, and numerous industrial processes. Growing efforts have focused on materials engineering strategies (e.g., superhydrophobicity) to prevent fouling. Here, we present a curious phenomenon in which crystals self-eject from heated, nanotextured superhydrophobic materials during evaporation of saline water drops. These crystal structures (crystal critters) have exceedingly minimal contact with the substrate and thus pre-empt crystal fouling. This unusual phenomenon is caused by cooperative effects of crystallization, evaporative flows, and nanoscale effects. The temperature dependence of the critter effect can be predicted using principles of mass conservation, and we demonstrate that self-propulsion can be generated via temperature gradients, which promote asymmetric growth. The insights on confinement-driven evaporative crystallization can be applied for antifouling by self-ejection of mineral foulants, for drop-based fluidic machines, or even for self-propulsion.

INTRODUCTION

Many of the uses for water are intimately familiar to us. Drinking water, wash water, water for agriculture, and even water used for recreation have an omnipresent and essential impact on our lives. However, water's impact and importance extend far beyond these everyday uses. In many developed countries, thermoelectric power production is one of the largest sources of water consumption (*1*), where it is used to cool reactors and transport heat. In 2015, 41% of all surface water withdrawals in the United States went toward cooling in thermoelectric power plants (*2*). Thermoelectric power accounts for 90% of all electricity generated within the United States and encompasses many forms of power production, including nuclear, coal, natural gas, and oil.

In its role as a coolant, water is sprayed on, flown through, or otherwise placed in contact with hot equipment (pipes, tanks, reactors, etc.). Many cooling processes use evaporation as a vital part of heat exchange due to the large heat transfer associated with phase change. However, when water is evaporated, contaminants within the water (including minerals) will precipitate at the point of evaporation. Over time, accumulation of these impurities reduces heat transfer performance, blocks pipes, and generally causes material corrosion and deterioration (*3*). Mineral fouling, in particular, is a leading cause of equipment degradation and failure in heat exchange processes (*4*).

To prevent mineral fouling, considerable effort and monetary investment goes toward pretreatment of coolant water using technologies such as ion exchange and reverse osmosis (*2*). Because of the ever increasing importance of water conservation (*5*), more and more water for thermoelectric cooling is being sourced from saline surface waters or from desalination waste brines rather than from freshwater sources (*6*), despite the associated increases in pretreatment costs. Surface engineering for control of salt-substrate interactions is therefore becoming increasingly attractive as a cost-effective alternative to pretreatment for preventing mineral fouling (*7*). The wetting properties of a material (also known as hydrophobicity and superhydrophobicity) have been the major focus of investigations seeking to eliminate fouling via surface engineering (*8*). However, mineral fouling is a multiphase problem, and interactions between the crystal and substrate and between the crystal and liquid are equally important for determining fouling propensity as are the interactions between the liquid and substrate (typically characterized by the contact angle) (*9*–*11*).

One method of examining interactions between a liquid, surface, and crystallizing solute is via drop evaporation. Traditionally, drop evaporation experiments are motivated by applications in self-assembly, inkjet printing, and sensing/diagnostics (*12*, *13*). Previous investigations have demonstrated that this technique can also be used as a method of exploring crystal adhesion and interfacial properties (*11*) and can inform on how damage to surfaces caused by crystallization occurs (*14*). Interfacial properties (*15*) and nucleation barriers (*16*) associated with different crystal chemistries control deposit morphologies, allowing us to draw inferences regarding the antifouling properties of a material from drop evaporation experiments.

Evaporating a drop of a volatile liquid containing a nonvolatile solute will induce crystallization of said solute due to rising concentrations, which eventually exceed the solubility limit. For solutes of low solubility, the patterns left by evaporative crystallization are similar to "coffee-ring" patterns formed by evaporation of a particle-laden drops (*11*, *12*, *16*). However, when the dissolved mass is excessive, three-dimensional crystal structures may arise (*17*, *18*). In particular, when a drop containing saturated sodium chloride is evaporated on a hydrophobic surface, "salt globes" form because of the propensity of crystals to nucleate at the air/water interface (*18*). These globes replicate the shape of the evaporating drop after reaching the solubility limit.

Here, we report an unexpected and unusual phenomenon in which crystal structures formed from evaporating drops of water saturated with sodium chloride self-eject from heated, superhydrophobic surfaces (*19*, *20*). This self-ejection occurs via the growth of crystalline "legs" during the end phase of evaporation, which cause the entire crystal structure to eject from the surface (*21*). We term

[1]Department of Mechanical Engineering, Massachusetts Institute of Technology, 77 Massachusetts Ave., Cambridge, MA 02141, USA. [2]Department of Mechanical and Aerospace Engineering, Princeton University, Princeton, NJ, 08540 USA.
*Corresponding author. Email: varanasi@mit.edu

the resulting structures composed of the salt globe and legs "crystal critters" due to the eerie motions produced during self-ejection and to the resemblance of the crystal structures to biological forms (*19*, *20*). This remarkable effect could enable design of extreme antifouling systems for spray cooling of hot surfaces using concentrated brines produced during desalination. This effect is also of interest for drop levitation/transport applications, which have traditionally been accomplished by heating surfaces to temperatures far in excess of the fluid boiling point (*22*). In such Leidenfrost levitation, evaporative flows create a lubricating vapor cushion between the drop and surface (*22*). In contrast, the critter effect occurs at much lower temperatures (60° to 100°C) than previously observed in both the traditional Leidenfrost effect (200°C) and even for cold-regime Leidenfrost on superhydrophobic materials (~130°C) (*23*–*25*). We demonstrate that this low-temperature ejection is accomplished via cooperative effects of crystallization, evaporative flows, and nanoscale phenomena.

RESULTS

Our experiments involve evaporation of a 5-μl drop of water containing sodium chloride (NaCl) dissolved to its solubility limit on a nanotextured superhydrophobic surface heated to a temperature T (Fig. 1A). We call this texture "nanograss," which is a low solid fraction texture composed of pointed grass-like features and valleys as shown in Fig. 1B (*26*). Because the initial solution is saturated with respect to salt (concentration = C_{sat}), volumetric losses of water due to evaporation (V_{evap}) lead to a corresponding increase in the mass of precipitated crystal: $M = C_{sat}V_{evap}$. The immediate growth of crystals is shown in the first image of Fig. 1C, where salt crystals have grown only a few seconds after drop deposition on nanograss heated to 90°C. Salt crystals accumulate at the air/water interface (*11*, *27*) instead of at the substrate or at the triple-phase contact line to form globe-like structures (*18*) that are reminiscent of the liquid marble effect (*28*).

The critter effect occurs during the second stage of evaporation. Following formation of the salt globe, there comes a time when remaining water suddenly dewets from the substrate due to preferential wetting of the newly formed mass of hydrophilic salt crystals. We call this moment the liftoff time (t_{lift}), and an example of this moment is shown in the second image of Fig. 1C. After this time, water contact is confined to the points where crystals touch the substrate. Continuous evaporation at the substrate surface induces an evaporative flow of water from the upper portion of the salt structure toward the substrate. As a result of this flow, crystalline legs develop at these contact points and continue to grow in length until the evaporation of water is complete. We call this second stage of evaporation the growth phase (t_{grow}, so that total evaporation time $t_{evap} = t_{lift} + t_{grow}$), as shown in the last two panels of Fig. 1C.

The contact points between the crystal structure and substrate shown in Fig. 1C branch into multiple legs and taper off toward the end of evaporation in a way that is similar to the growth of salt trees from evaporating salt solutions (*29*). This tapering effect is due to there being less water (and therefore less dissolved salt) near the end of the process. The resulting structure is a crystal globe balanced on legs with limited (or no) adhesion to the substrate. The image in the last column of Fig. 1C shows a gap between the substrate and salt structure and has only two locations where legs contact the surface. Because of this minimal contact, crystal critters are easily removed and will occasionally roll away on their own during or after evaporation (see movie S1).

The critter effect is a strong function of temperature, as shown in Fig. 1 (D) and (E). Below substrate temperatures of ~50°C, we did not observe either the dewetting event or the subsequent leg growth

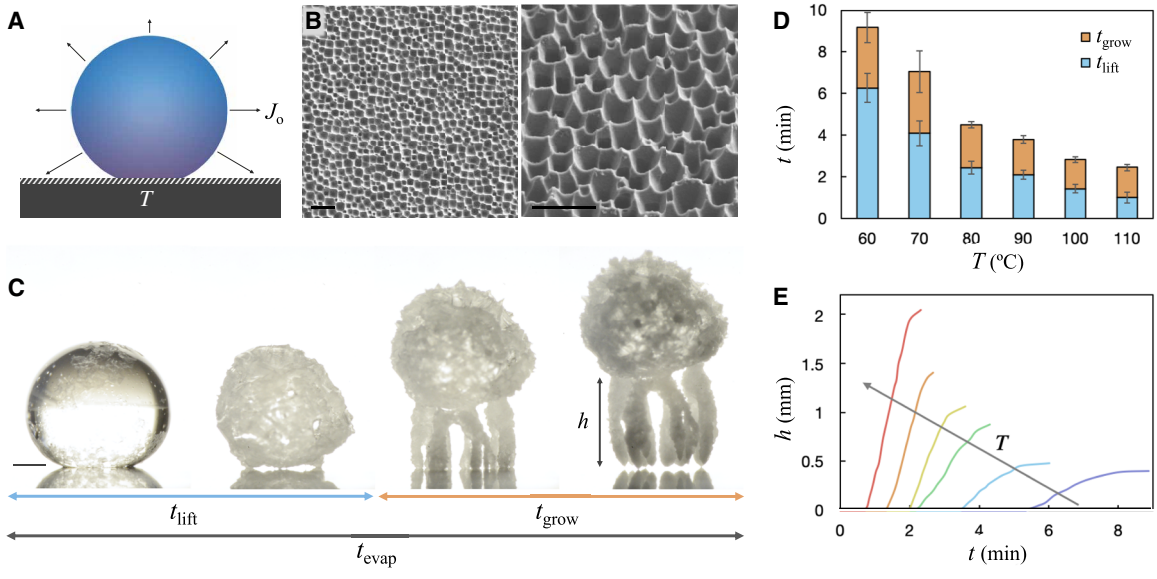

Fig. 1. Growth of crystal critters. (**A**) Schematic of experiment, where a drop of water containing dissolved salt is evaporated on a hot, superhydrophobic substrate. (**B**) Scanning electron microscopy (SEM) images showing nanotexture of superhydrophobic nanograss surface. Scale bars, 3 μm. (**C**) Growth of crystal critters from a 5-μl drop with time at a substrate temperature of 90°C. Scale bar, 0.5 mm. (**D**) Time for evaporation as a function of temperature. Entire bar represents the total evaporation time, the blue segment is the first stage of evaporation before leg growth, and the orange segment is the second stage of evaporation during which legs grow. (**E**) Growth of legs with time as a function of temperature, where the lowest temperature (purple, right-most line) is 60°C and hottest (red, left-most line) is 110°C.

associated with crystal critter formation. Note, however, that vertical ejection of crystals has been observed at lower temperatures in a related effect on smooth surfaces (see note S1 for more on smooth surfaces) (*21*). The apparent temperature limit for critter formation may be related to the enhanced stability of the air/vapor layer within superhydrophobic textures at elevated temperatures (*25*, *30*–*32*) and hints that the importance of the air layer in triggering the dewetting event leads to critter growth. At substrate temperatures above the apparent limit of ~50°C, critter growth becomes more marked. As would be expected, evaporation time decreases with increased temperature. The ratio between the time before liftoff and the growth time also decreases with increased temperature (Fig. 1D). Thus, critters formed on hotter substrates tend to liftoff earlier than those on cooler substrates, as shown in Fig. 1E. The growth rate (the slope in Fig. 1E) also significantly increases with substrate temperature, leading to larger final leg heights on the hotter substrates.

We now seek to understand the growth of the critter legs at the nanograss interface. Drops are suspended on the peaks of the nanograss features so that a layer of air (plastron) within the pore/valleys separates the liquid from the substrate, as shown in Fig. 2 (A) and (B) (left) (*33*). However, unlike some microscale textures fabricated using masks for highly controlled features, this texture is also somewhat stochastic and exhibits minor variations in the pore size, pore depth, local geometry, and height of the peak features (see Fig. 1B and inset of Fig. 2A). Thus, while a majority of the drop is suspended on the grass-like peaks, material stochasticity (especially where regions of locally lower peak height and higher valley floors coexist) and/or stochasticity during drop placement may enable local displacement of the air layer and impalement of water in the texture pores. The right side of the schematic in Fig. 2B illustrates such localized impalement, while the left illustrates the suspended case expected to comprise the majority of the contact area between the drop and substrate.

We image the interface between a drop and the nanograss surface via optical microscopy (shown in Fig. 2C). This image, showing a top-down view shortly after drop placement, reveals a number of small dimples that appear to show local fluid impalement into the texture. The largest of these dimples has an approximate diameter of ~250 to 300 μm, with a number of smaller dimples visible but poorly resolved at the macroscale of the 5-μl drop. We hypothesize that it is in these areas with maximum solid-liquid contact that crystal legs will grow. However, note that not all of the dimpled regions in Fig. 2C will necessarily form legs. As shown in Fig. 1, the dewetting event that triggers critter growth reduces liquid/substrate contact to only those locations where crystals rest on the surface. Legs will therefore only grow at locations with both local impingement and that also remain in contact with the crystal globe after t_{lift}.

Following critter growth and ejection, substrates were imaged using scanning electron microscopy (SEM) (Fig. 2, D and E). Figure 2E reveals a number of salt stains ranging in diameter from 10 to 270 μm. A majority of stains are on the smaller end of this spectrum, with one large stain having a diameter of 270 μm. The agreement between the estimated size of the optically observed dimples and the size of the largest stain (note that the regions correlated to the smaller stains would not be visible in Fig. 2C) provides further evidence that these regions are the same. A closer inspection of a particular salt stain is shown in Fig. 2D, where the inset shows that the stains are composed of small amounts of residue within the substrate nanopores. The presence of the salt residue does not alter the apparent wettability or heat transfer between the substrate and drop, enabling indefinite repetition of critter growth at a given location. See fig.S2 for more examples of residue stains and figs. S3 and S4 for more images of legs.

Movies of crystal critter growth clearly show water flow (indicated by bubble movement) toward the substrate through the legs (see movie S2), suggesting that legs are hollow, crystalline tubes. Figure 2F shows an optical image of the region between a fully evaporated crystal critter and the substrate, where the yellow outline highlights a location where the bottom portion of a leg has been left on the substrate. A similar structure is imaged by SEM and shown in Fig. 2G, confirming that critter legs appear to be hollow tubes. These tube-like

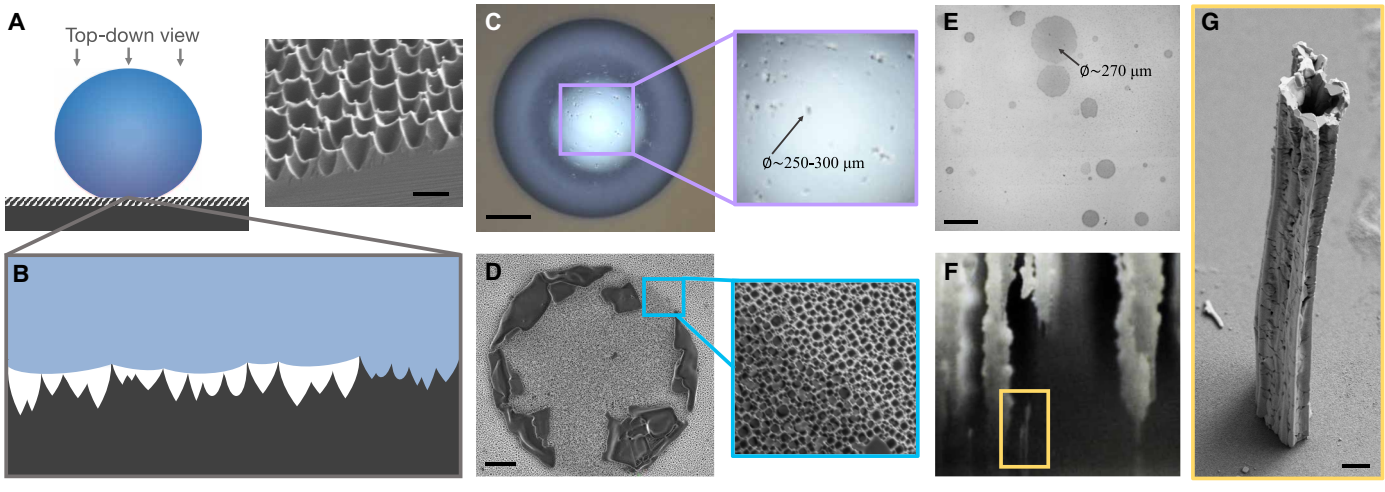

Fig. 2. Crystal critter legs are tubes. (**A**) Schematic showing drop on nanograss surface. Inset is SEM image showing pore geometry of the nanograss. Scale bar, 2 μm. (**B**) Illustration of nanograss texture. Most of the drop rests on a layer of plastron within the superhydrophobic texture, but liquid may impinge in small, localized areas. (**C**) Top view of a drop immediately after placement on a surface showing small, localized areas where liquid is impaled within the texture. Scale bar, 1 mm. (**D**) SEM image showing detail of a salt stain where the outer perimeter has also been deposited. The outer diameter is ~32 μm, and the inner diameter is ~25 μm. Scale bar, 5 μm. (**E**) SEM image of a region where salt stains reveal where critter legs previously grew. Scale bar, 200 μm. (**F**) Optical image of critter legs near surface, where a small tube still connected to the surface is outlined in yellow. (**G**) SEM image of the bottom of a tube left behind on a surface. Scale bar, 20 μm.

legs grow in a way that mirrors the coffee-ring effect observed for evaporating drops but on a markedly smaller scale. In the coffee-ring effect, a drop evaporating on a substrate leaves a ring deposit due to radial flow transporting particles toward the contact line (*12*). Here, evaporation is confined to the localized impalement points shown in Fig. 2 (C) and (E). Evaporative flow transports salt to these points to create circular deposits (such as the one in Fig. 2D). The deposit grows outward and is simultaneously pushed upward due to evaporative flow and to growth of new crystals at the bottom of the tube. Thus, as a given crystalline ring grows horizontally, it also moves vertically (away from the substrate), and the resulting leg structure is that of a cone. Water moves down this conical tube toward the substrate until growth terminates due to complete vaporization of the water.

Statistics on the occurrence of different number of legs (Fig. 3A) for a given crystal critter, and on the size of the legs (Fig. 3B) were compiled. The number of legs is seemingly random, which follows from the hypothesis that legs form at positions of local fluid impalement into substrate texture at the liftoff time, which is expected to be variable. A given crystal critter will form several legs if there are several such points, and fewer legs form when there are fewer impalement points. The statistics on leg diameters (i.e., diameters of the impalement points) exhibit a more structured distribution with a majority of legs having a diameter between 10 and 40 μm. The median diameter is 30 μm.

To better understand this phenomenon, experiments were conducted on additional substrate textures (Fig. 4). Untextured hydrophobic surfaces (Fig. 4A, light gold line of Fig. 4F) did not exhibit formation of distinctive legs in these experiments. However, a small amount of vertical "lift" of the crystal structure is shown in Fig. 4A, as evidenced by the difference in the maximum deposit height in the intermediate and final time points (see note S1 and fig. S1 for more time points). Liftoff and ejection on smooth materials have been previously shown in cases where the crystal does not pin to the underlying substrate during the initial phases of evaporation (*21*). Pinning during evaporative crystallization from drops is largely a function of interfacial properties (*11*, *21*), which will also dictate whether vertical growth occurs. As with the critter effect, the vertical lift on smooth hydrophobic surfaces toward the end of evaporation can be attributed to capillary bridges formed between crystals and the substrate (*21*). Similarly, the rate of vertical ejection on smooth surfaces increases with increased substrate temperature; an effect that has previously been attributed to a temperature-dependent crystal growth (*21*). However, in the present experiments on smooth surfaces, we do not observe a discernable t_{lift} at which water markedly dewets from the substrate and triggers leg growth (as shown in Fig. 1C).

As previously established, superhydrophobic nanograss (texture length scale, ~0.1 to 1 μm) (Fig. 4B, green line of Fig. 4F) successfully forms critters. However, another superhydrophobic texture composed of regularly spaced microposts with a texture length scale of 10 μm exhibits no vertical growth or ejection phenomena (Fig. 4C, dark gray line of Fig. 4F), despite having a contact angle similar to that of the nanograss texture. The drop starts in the Cassie state (suspended on the microposts) but slowly slides into the Wenzel state (impaled between the posts) as evaporation proceeds (see intermediate timestep in Fig. 4C) (*34*). The slow transition and subsequent radial spreading shown in Fig. 4F are in stark contrast to the fast transition typically observed for the breakdown of superhydrophobicity on micropost textures (*35*). Horizontal spreading and transition to the impaled Wenzel state is also observed on a micropost surface with a hierarchical nanograss texture (Fig. 4D, black line of Fig. 4F), indicating that the microscale texture disrupts the critter effect despite the presence of the nanoscale texture. Experiments on a superhydrophobic microhole substrate with 10-μm square holes (Fig. 4E, lavender line of Fig. 4F) also fail to form crystal critters. This final result suggests that it is the length scale of the texture that is important in the critter effect rather than by some vapor-trapping effect due to the valley-like structure of the nanograss pores.

The absence of vertical growth and ejection on superhydrophobic surfaces with microscale textures can be attributed to crystallization within those textures (Fig. 4G). Crystallization at the microscale air/water interface induces lateral flow due to the hydrophilicity of newly nucleated salt crystals (*14*), which then drastically influences the transition between the Cassie and Wenzel states (*36*). This observation is consistent with previous studies exploring evaporation of sodium chloride solution on heated, superhydrophobic surfaces in which no liftoff/ejection occurred (*18*, *21*). Similarly, on the hierarchical texture composed of nanograss-topped microposts, crystal growth within (and/or settling into) the texture causes impalement of the meniscus, and salt crystals appear in the valleys of the texture. The changes to wettability induced by crystallization within the microscale textures lead to more lateral spreading of salt crystals on the superhydrophobic surfaces than is observed for the smooth hydrophobic material, as shown in Fig. 4F.

In contrast to the microtextured surfaces, lateral spreading is avoided on the nanograss substrate due to confinement effects where liquid/solid contact is confined to the locally impaled regions shown in Fig. 2. Because these regions are exceedingly small, any crystals that form at the triple-phase contact line (see the small coffee ring–like morphology shown in Fig. 2D) will also be limited in size and will not trigger macroscopic breakdown of superhydrophobicity. Crystals that form elsewhere at the air/water interface between the

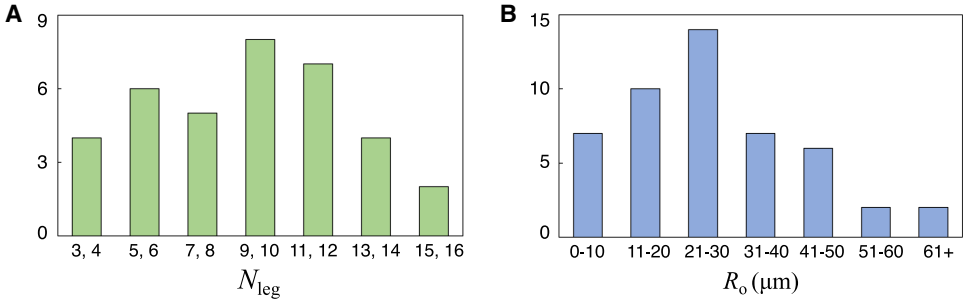

Fig. 3. Statistics on critter legs. (**A**) Distribution of the number of legs across different critter structures. (**B**) Distribution showing outer radius of salt stains.

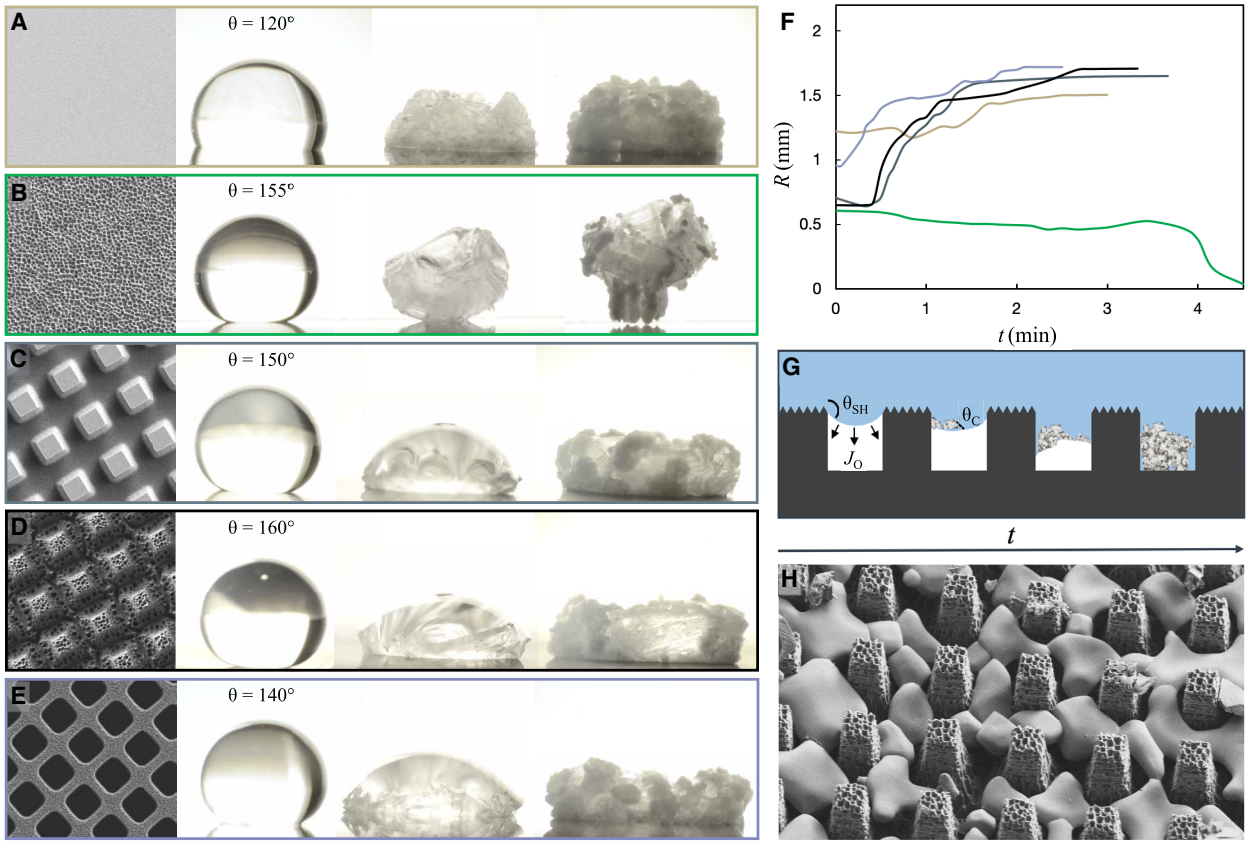

Fig. 4. Critters grow due to nanoscale confinement. From left to right, images in (A) to (E) show SEM of substrate texture, initial drop contact angle, intermediate step where crystals have begun to form, and final crystalline deposit formed by evaporation on substrates heated to 70°C for (**A**) hydrophobic smooth silicon, (**B**) superhydrophobic nanograss (i.e., the same texture used in Figs. 1 and 2), (**C**) superhydrophobic microposts, (**D**) superhydrophobic microposts further textured with nanograss, and (**E**) superhydrophobic microholes. SEM images for (A) to (E) are 50 μm wide. (**F**) Contact line radius with time for each substrate. Green line shows superhydrophobic nanograss surface, light gold line shows hydrophobic untextured surface, dark gray corresponds to the superhydrophobic micropost surface, black corresponds to the superhydrophobic nano-micro composite surface, and lavender to the superhydrophobic microholes. (**G**) Illustration showing process of crystal intrusion into microtextures that leads to the Cassie-Wenzel transition on micropost surfaces. (**H**) SEM image of salt deposit inside the microtexture of the superhydrophobic microposts and nanograss substrate (D).

substrate and liquid (i.e., locations where the drop is suspended by the nanograss) do not pin to the low solid fraction nanograss tips nor settle into/onto the texture as they do for the microscale texture. This effect can be attributed to the increased stability of the plastron and of superhydrophobicity for the nanofeatured texture. The lack of the lack of crystallization and pinning at the solid/liquid interface within the nanograss valleys even in the impaled regions is due to both the hydrophobic chemistry of the surface (*11*) and to smaller-scale surface confinement/geometry effects that can drastically alter crystal nucleation and growth (*37*, *38*). A similar effect has been observed for ice nucleation on a nanograss texture, in which ice crystals within the nanoscale texture were unable to grow (*39*). Crystal intrusion into the microscale texture of the hierarchal micropost surface but not within the nanoscale texture is shown in the SEM image of Fig. 4H, confirming the importance of confinement effects for the critter phenomena.

The confinement effects and the stability of the air layer on the nanograss substrate prevent crystallization-induced breakdown of superhydrophobicity and enable the dewetting event that triggers critter formation. These effects ultimately lead to the growth of crystalline legs and self-ejection during the growth phase of critter formation. Under the current experimental conditions with evaporative flux and microscopic length scales, sodium chloride crystallization is expected to be transport limited rather than kinetically limited (*40*). Thus, the evaporation rate will have a critical influence on the rate of crystallization (*27*, *41*). We therefore suggest a model for the effect based on an evaporative flow confined to areas between the cylindrical crystalline legs and the substrate (see Fig. 5A for geometry). Assuming that all evaporation occurs at the contact line between the legs and substrate, a mass balance for the fluid can be written as

$$\frac{dV}{dt} = -(2\pi R_o N) J_o$$
$$J_o = \frac{D_{vap} \Delta C_{cap}}{\rho} \quad (1)$$

Where dV/dt is volumetric evaporative flow, R_o is the outer radius of a leg, N is the number of legs, and J_o is the evaporative flux. We have taken the form of evaporative flux for the case in which evaporation is diffusion limited in the vapor phase. The evaporative flux is a function of the diffusion of water vapor in air (D_{vap}) and the concentration gradient of vapor in air (ΔC_{vap}). Both of these depend

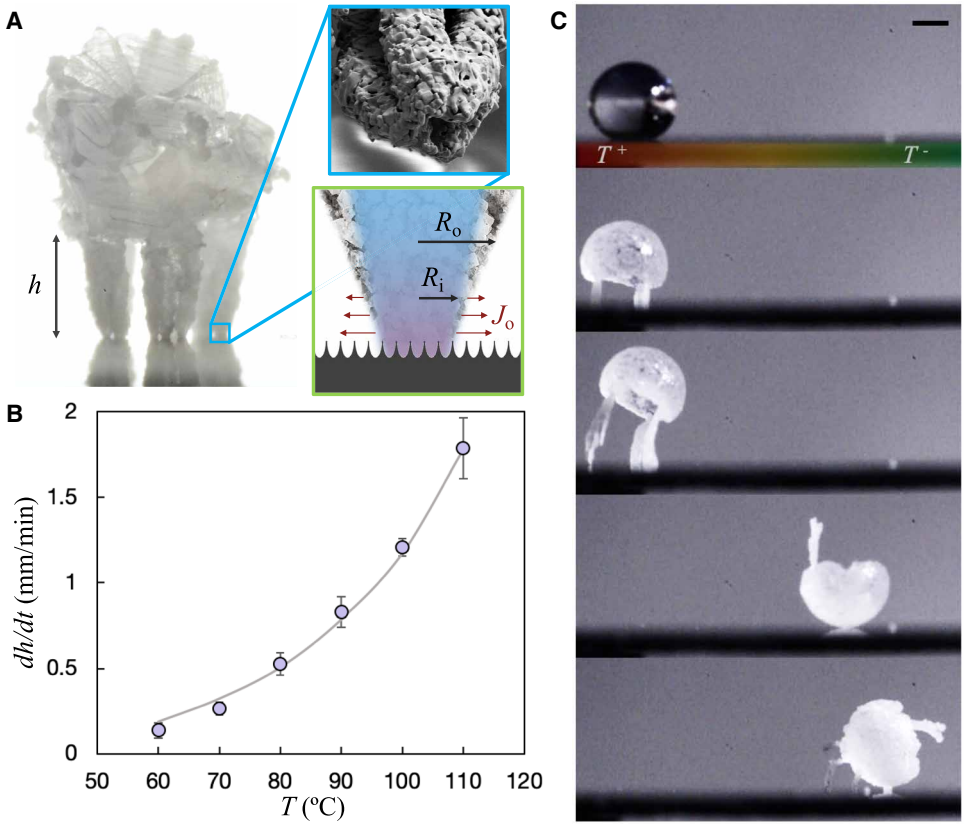

Fig. 5. Temperature-dependent growth of critter legs. (**A**) Images defining model parameters including h (length of the legs), R_o, and R_i (outer and inner diameter of a given leg). (**B**) Average leg growth rate (millimeters per minute) as a function of substrate temperature, where purple circles indicate experimental values averaged from five to six trials, error bars show SD, and solid line is the model of Eq. 3 (where $R_o = 16$ μm and $R_i = 12.5$ μm). (**C**) Experiment showing critter growth on a substrate with an imposed temperature gradient. Legs grow longer on the side with a higher temperature, causing the crystal critter to become more and more unstable until it eventually tips over and rolls in the direction of the lower temperature. New legs begin to grow at the new position until evaporation is complete. Scale bar, 1 mm.

on vapor temperature, which can be approximated as the substrate temperature (see note S2 for more information and table S1 for data). For simplicity, we assume that all N legs have the same outer radius, although we know from experimental evidence (Figs. 2E and 3B) that there is some variability across leg diameters.

Next, we consider a mass balance of the salt and assume that salt concentration within the drop remains constant at the saturation concentration. Thus, the precipitation rate is equal to the saturation concentration multiplied by the evaporation rate. Approximating the legs as cylindrical tubes with an inner diameter R_i, we obtain

$$N\rho_c\pi(R_o^2 - R_i^2)\frac{dh}{dt} = -C_{sat}\frac{dV}{dt} \quad (2)$$

Where dh/dt is the growth rate of the crystalline tubes and ρ_c is the density of the crystals (see Fig. 5A). Combining Eqs. 1 and 2, we arrive at the growth rate of the legs

$$\frac{dh}{dt}\left(\frac{2R_o}{R_o^2 - R_i^2}\right)\frac{C_{sat}J_o}{\rho_c} \quad (3)$$

Equation 3 has several features that are observed experimentally, including that dh/dt is independent of number of legs and increases with increasing temperature (J_o). We test this prediction against experimental data using the geometry from the deposit shown in Fig. 2D as an example of a typical deposit size (R_o = 16 μm and R_i = 12.5 μm). The salt density (ρ_c = 2160 kg/m^3 for NaCl) and saturation concentration (C_{sat} = 357 kg/m^3) are constant so that dh/dt is a function of evaporative flux (and therefore substrate temperature) only. This model is plotted against experimental data in Fig. 5B with very good agreement, although it should be noted that different leg geometry (R_o and R_i) may shift the relative value of this plot. The overall trend with temperature, however, will not be altered by this choice.

Because leg growth rate increases with temperature, it is possible to induce directional rolling by applying a temperature gradient across the substrate. This is shown in Fig. 5C, where a critter is grown on a substrate with an imposed temperature gradient. Legs grow shorter on the side with a lower temperature and longer on the side with the higher temperature. This asymmetrical growth causes the crystal structure to tip and roll in the direction of lower temperature. At this point, water is not fully evaporated, and the remaining water continues to evaporate via formation of new legs at the second location. Crystal structures can roll two or even three times before complete evaporation (see movie S3).

DISCUSSION

We have introduced and explained an unusual behavior exhibited by evaporating drops of saturated sodium chloride on heated, nanotextured superhydrophobic surfaces, in which salt structures self-eject via growth of legs. This effect is trigged by the dewetting of water from the low solid fraction substrate in favor of wetting salt crystals previously grown at the air/water interface. This dewetting event is only possible due to confinement of both crystallization and evaporative flows induced by nanotexture and will not occur for superhydrophobic surfaces composed of microscale features (*18*, *21*). Confinement and a dearth of adhesion point also enable ejection at lower temperatures than previously observed for evaporation-induced drop levitation (*23*–*25*).

In addition to being innately interesting, the crystal critter effect has potential application for improving sustainability in spray cooling heat exchange by introducing a strategy for eliminating crystal adhesion on hot surfaces. By taking advantage of the effect, it may be possible to directly use saline waters as a heat transfer fluid while also avoiding mineral fouling of the heat exchange surface. Using saltwater rather than fresh water for cooling applications simultaneously reduces costs associated with water treatment while also preserving fresh water for other vital purposes. Furthermore, one might also imagine a new type of cogeneration plant in which desalinated seawater is produced as a by-product of heat exchange by recovering water vapor produced during critter formation.

Another potential use for the effect could be for treatment of waste brines in zero liquid discharge systems, where complete recovery of water from very salty reverse osmosis reject water is challenging due to the difficulties in working with high salinity brines. Self-ejection of salt foulants is also of particular importance for marine vessels and coastal structures (*42*), where deposition of salt and subsequent crystal growth from seaspray is a leading cause of damage (*43*). More broadly, these insights on confinement-driven evaporative crystallization could also be applied for novel drop-based fluidic machines (*44*) or for self-propulsion (*24*, *45*–*47*).

MATERIALS AND METHODS

Water preparation

Saturated sodium chloride (NaCl) solutions were prepared by adding sodium chloride salt (Sigma-Aldrich) to a volume of deionized water. The mass of sodium chloride used was in excess of the saturation concentration of the salt in water (357 g/liter at 20°C) so that the total mass was unable to fully dissolve. The solution was mixed for a period of several hours to enhance salt dissolution before filtration of excess solid using vacuum filtration.

Substrate preparation

The nanograss texture, also termed black silicon, was prepared by reactive ion etch, as described previously (*26*). The texture was then hydrophobized by vapor deposition of a fluorosilane chemistry [trichloro (1*H*,1*H*,2*H*,2*H*-perfluorooctyl)] over a period of 6 hours. Preparation of other textures has been described previously (*36*).

Experiments

Functionalized substrates were heated on a hot plate to the specified temperature, and a thermocouple was used to confirm the temperature of both the hot plate and substrates. Five-microliter drops of saturated sodium chloride solution were then gently pipetted onto the heated substrates. Substrates had to be completely level to avoid drop rolling during deposition. A camera mounted to a tripod equipped with a Navitar lens was focused on the drops, and evaporation was recorded for the duration. Experiments were repeated between five and seven times per temperature and were performed in a temperature-controlled lab environment with relative humidity between 38 and 44%. The temperature gradient experiment of Fig. 5C was performed by clamping one end of a long (50 mm) superhydrophobic nanograss substrate to a hot plate heated to 120°C and the other end to a Peltier cooling stage cooled to 0°C. Drops were deposited at a position with a temperature near 90°C and typically rolled once or twice toward a lower temperature position of between 55° and 75°C, depending on the number of rolls.

Modeling

The form of evaporative flux given by Eq. 1 describes the situation in which evaporation is limited by diffusion in the vapor phase (*48*). The values used for the diffusion coefficient of water in air and for the saturated vapor concentration of water in air as a function of temperature are given in the Supplementary Materials (table S1), along with the value of the evaporative flux calculated from Eq. 1 (neglecting variations of water density with temperature, $\rho = 1000\ kg/m^3$).

Images

The optical images of crystal critters or other crystal structures (Figs. 1C; 4, A to E; and 5A) were taken from still frames of movies recorded on a Nikon camera equipped with a Navitar lens or a macro lens (Fig. 5C). Minor brightness/contrast adjustments were made uniformly. SEM images were captured using a Zeiss Ultra55 SEM. The secondary electron detector (better for capturing structure detail) was used for Figs. 1B, 2G, and 4 (A) to (E) and (H), and the inset of Fig. 5A, while the InLens detector (better for enhanced contrast between different chemistries/structures) was used for Fig. 2 (A) and (E).

SUPPLEMENTARY MATERIALS

Supplementary material for this article is available at http://advances.sciencemag.org/cgi/content/full/7/18/eabe6960/DC1

REFERENCES AND NOTES

1. K. Averyt, J. Macknick, J. Rogers, N. Madden, J. Fisher, J. Meldrum, R. Newmark, Water use for electricity in the United States: An analysis of reported and calculated water use information for 2008. *Environ. Res. Lett.* **8**, 015001 (2013).
2. S.-Y. Pan, S. W. Snyder, A. I. Packman, Y. J. Lin, P.-C. Chiang, Cooling water use in thermoelectric power generation and its associated challenges for addressing water-energy nexus. *Water Energy Nexus.* **1**, 26–41 (2018).
3. X. Zhao, X. D. Chen, A critical review of basic crystallography to salt crystallization fouling in heat exchangers. *Heat Transf. Eng.* **34**, 719–732 (2013).
4. V. S. Sastri, *Challenges in Corrosion* (John Wiley & Sons, Inc, Hoboken, NJ, USA, 2015), pp. 95–126.
5. T. J. Feeley III, T. J. Skone, G. J. Stiegel Jr., A. McNemar, M. Nemeth, B. Schimmoller, J. T. Murphy, L. Manfredo, Water: A critical resource in the thermoelectric power industry. *Energy* **33**, 1–11 (2008).
6. C. Zhang, L. Zhong, J. Wang, Decoupling between water use and thermoelectric power generation growth in China. *Nat. Energy* **3**, 792–799 (2018).
7. S. Daer, J. Kharraz, A. Giwa, S. W. Hasan, Recent applications of nanomaterials in water desalination: A critical review and future opportunities. *Desalination* **367**, 37–48 (2015).
8. M. Ferrari, A. Benedetti, Superhydrophobic surfaces for applications in seawater. *Adv. Colloid Interface Sci.* **222**, 291–304 (2015).
9. J. Macadam, P. Jarvis, Chapter 1 - Water-Formed Scales and Deposits: Types, Characteristics, and Relevant Industries, in *Mineral Scales and Deposits*, Z. Amjad, K. D. Demadis, Eds. (Elsevier, 2015), pp. 3–23.

10. G. Azimi, Y. Cui, A. Sabanska, K. K. Varanasi, Scale-resistant surfaces: Fundamental studies of the effect of surface energy on reducing scale formation. *Appl. Surf. Sci.* **313**, 591–599 (2014).
11. N. Shahidzadeh, M. F. L. Schut, J. Desarnaud, M. Prat, D. Bonn, Salt stains from evaporating droplets. *Sci. Rep.* **5**, 10335 (2015).
12. R. D. Deegan, O. Bakajin, T. F. Dupont, G. Huber, S. R. Nagel, T. A. Witten, Capillary flow as the cause of ring stains from dried liquid drops. *Nature* **389**, 827–829 (1997).
13. R. D. Deegan, O. Bakajin, T. F. Dupont, G. Huber, S. R. Nagel, T. A. Witten, Contact line deposits in an evaporating drop. *Phys. Rev. E* **62**, 756–765 (2000).
14. J. Desarnaud, D. Bonn, N. Shahidzadeh, The pressure induced by salt crystallization in confinement. *Sci. Rep.* **6**, 30856 (2016).
15. N. Shahidzadeh-Bonn, S. Rafai, D. Bonn, G. Wegdam, Salt crystallization during evaporation: Impact of interfacial properties. *Langmuir* **24**, 8599–8605 (2008).
16. S. A. McBride, R. Skye, K. K. Varanasi, Differences between colloidal and crystalline evaporative deposits. *Langmuir* **36**, 11732–11741 (2020).
17. M. J. Qazi, H. Salim, C. A. W. Doorman, E. Jambon-Puillet, N. Shahidzadeh, Salt creeping as a self-amplifying crystallization process. *Sci. Adv.* **5**, eaax1853 (2019).
18. B. Shin, M.-W. Moon, H.-Y. Kim, Rings, igloos, and pebbles of salt formed by drying saline drops. *Langmuir* **30**, 12837–12842 (2014).
19. S. McBride, H.-L. Girard, K. Varanasi, *72th Annual Meeting of the APS Division of Fluid Dynamics - Gallery of Fluid Motion* (American Physical Society, 2019); https://gfm.aps.org/meetings/dfd-2019/5d7bfb59199e4c429a9b2da8.
20. S. A. McBride, H.-L. Girard, K. K. Varanasi, Crystal critters. *Phys. Rev. Fluids* **5**, 110508 (2020).
21. H. Salim, P. Kolpakov, D. Bonn, N. Shahidzadeh, Self-lifting NaCl crystals. *J. Phys. Chem. Lett.* **11**, 7388–7393 (2020).
22. D. Quéré, Leidenfrost dynamics. *Annu. Rev. Fluid Mech.* **45**, 197–215 (2013).
23. P. Bourrianne, C. Lv, D. Quéré, The cold Leidenfrost regime. *Sci. Adv.* **5**, eaaw0304 (2019).
24. G. Dupeux, P. Bourrianne, Q. Magdelaine, C. Clanet, D. Quéré, Propulsion on a superhydrophobic ratchet. *Sci. Rep.* **4**, 5280 (2015).
25. I. U. Vakarelski, N. A. Patankar, J. O. Marston, D. Y. C. Chan, S. T. Thoroddsen, Stabilization of Leidenfrost vapour layer by textured superhydrophobic surfaces. *Nature* **489**, 274–277 (2012).
26. C. Dorrer, J. Rühe, Wetting of silicon nanograss: From superhydrophilic to superhydrophobic surfaces. *Adv. Mater.* **20**, 159–163 (2008).
27. S. Misyura, The dependence of evaporation and crystallization kinetics on dynamic and thermal background. *AIChE J.* **66**, e16282 (2020).
28. P. Aussillous, D. Quéré, Liquid marbles. *Nature* **411**, 924–927 (2001).
29. R. Du, H. A. Stone, Evaporatively controlled growth of salt trees. *Phys. Rev. E* **53**, 1994–1997 (1996).
30. I. U. Vakarelski, D. Y. C. Chan, J. O. Marston, S. T. Thoroddsen, Dynamic air layer on textured superhydrophobic surfaces. *Langmuir* **29**, 11074–11081 (2013).
31. G. Liu, L. Fu, A. V. Rode, V. S. J. Craig, Water droplet motion control on superhydrophobic surfaces: Exploiting the Wenzel-to-Cassie transition. *Langmuir* **27**, 2595–2600 (2011).
32. Y. Liu, X. Chen, J. H. Xin, Can superhydrophobic surfaces repel hot water? *J. Mater. Chem.* **19**, 5602 (2009).
33. D. Quéré, Leidenfrost becomes a fakir. *Nat. Mater.* **11**, 915–916 (2012).
34. S. Moulinet, D. Bartolo, Life and death of a fakir droplet: Impalement transitions on superhydrophobic surfaces. *Eur. Phys. J. E* **24**, 251–260 (2007).
35. M. Sbragaglia, A. M. Peters, C. Pirat, B. M. Borkent, R. G. H. Lammertink, M. Wessling, D. Lohse, Spontaneous breakdown of superhydrophobicity. *Phys. Rev. Lett.* **99**, 156001 (2007).
36. S. A. McBride, S. Dash, K. K. Varanasi, Evaporative crystallization in drops on superhydrophobic and liquid-impregnated surfaces. *Langmuir* **34**, 12350–12358 (2018).
37. B. D. Hamilton, J.-M. Ha, M. A. Hillmyer, M. D. Ward, Manipulating crystal growth and polymorphism by confinement in nanoscale crystallization chambers. *Acc. Chem. Res.* **414**, 414–423 (2012).
38. Q. Jiang, M. D. Ward, Crystallization under nanoscale confinement. *Chem. Soc. Rev.* **43**, 2066–2079 (2014).
39. S. Bengaluru Subramanyam, V. Kondrashov, J. Rühe, K. K. Varanasi, Low ice adhesion on nano-textured superhydrophobic surfaces under supersaturated conditions. *ACS Appl. Mater. Interfaces* **8**, 12583–12587 (2016).
40. A. Naillon, P. Duru, M. Marcoux, M. Prat, Evaporation with sodium chloride crystallization in a capillary tube. *J. Cryst. Growth* **422**, 52–61 (2015).
41. S. Y. Misyura, Evaporation and heat transfer of aqueous salt solutions during crystallization. *Appl. Therm. Eng.* **139**, 203–212 (2018).
42. K. M. Anwar Hossain, S. M. Easa, M. Lachemi, Evaluation of the effect of marine salts on urban built infrastructure. *Build. Environ.* **44**, 713–722 (2009).
43. K. A. Chandler, *Marine and Offshore Corrosion* (Butterworths, 1985).
44. N. J. Cira, A. Benusiglio, M. Prakash, Vapour-mediated sensing and motility in two-component droplets. *Nature* **519**, 446–450 (2015).
45. E. Bormashenko, Y. Bormashenko, R. Grynyov, H. Aharoni, G. Whyman, B. P. Binks, Self-propulsion of liquid marbles: Leidenfrost-like levitation driven by Marangoni flow. *J. Phys. Chem. C* **119**, 9910–9915 (2015).
46. G. Lagubeau, M. Le Merrer, C. Clanet, D. Quéré, Leidenfrost on a ratchet. *Nat. Phys.* **7**, 395–398 (2011).
47. A. Bouillant, T. Mouterde, P. Bourrianne, A. Lagarde, C. Clanet, D. Quéré, Leidenfrost wheels. *Nat. Phys.* **14**, 1188–1192 (2018).
48. H. Hu, R. G. Larson, Evaporation of a sessile droplet on a substrate. *J. Phys. Chem. B* **106**, 1334–1344 (2002).

Acknowledgments: Substrate textures were fabricated, and SEM images obtained using the facilities at the Harvard Center for Nanoscale Science. **Funding:** We are grateful for funding support from Equinor via the MIT Energy Initiative. S.A.M. acknowledges funding from the MIT Martin Fellowship Program and from the NSF GRFP grant no. 1122374. **Author contributions:** S.A.M., H.-L.G., and K.K.V. all contributed to these experiments, the analysis, and writing/editing of this manuscript. **Competing interests:** The authors declare that they have no competing interests. **Data and materials availability:** All data needed to evaluate the conclusions in the paper are present in the paper and/or the Supplementary Materials. Additional data related to this paper may be requested from the authors.

Submitted 8 September 2020
Accepted 9 March 2021
Published 28 April 2021
10.1126/sciadv.abe6960

Citation: S. A. McBride, H.-L. Girard, K. K. Varanasi, Crystal critters: Self-ejection of crystals from heated, superhydrophobic surfaces. *Sci. Adv.* **7**, eabe6960 (2021).

Crystal critters: Self-ejection of crystals from heated, superhydrophobic surfaces

Samantha A. McBride, Henri-Louis Girard and Kripa K. Varanasi

Sci Adv **7** (18), eabe6960.
DOI: 10.1126/sciadv.abe6960